Available online at www.sciencedirect.com
SciVerse ScienceDirect
Acta Materialia 60 (2012) 657–663
Acta MATERIALIA
www.elsevier.com/locate/actamat

Orientation selection in solidification patterning

Morteza Amoorezaei *, Sebastian Gurevich, Nikolas Provatas

Department of Materials Science and Engineering, McMaster University, Hamilton, ON, Canada L8S 4L7

Received 25 July 2011; received in revised form 29 September 2011; accepted 5 October 2011
Available online 22 November 2011

Abstract

Crystal growth has been recognized as a paradigm for non-equilibrium pattern formation for decades. Scientific interest in this field has focused on the growth rates and curvature of branches in snowflake-like structures patterned after a solid's crystallographic orientations. In reality, there exists a much richer variety of crystal patterns in nature. Investigations of dendritically solidifying alloys reveals structures that continuously change orientation between different growth directions, some of which are not along preferred crystallographic directions. The selection mechanism of such patterns is poorly understood. In this paper we demonstrate computationally and experimentally that a material's surface tension anisotropy can compete with anisotropies present in processing conditions during solidification to produce a continuous transition from dendritic to seaweed and fractal-like structures. The phase space of such morphologies is characterized and the selection principles of the various morphologies explored are explained. These results have direct relevance to microstructure formation in commercial lightweight metal castings.

Keywords: Orientation; Dendrite; Seaweed; Directional solidification; Phase field

1. Introduction

Dendritic solidification has been a well-accepted paradigm for many non-equilibrium interface pattern formation phenomena [1–11]. Dendritic microstructures are formed in most alloys during processes such as casting and welding. The complex patterns created by the dendritic network leave their signature on the distribution of secondary phases that form in the interdendritic spaces that contain supersaturated liquid pools due to solute rejection in the late stages of solidification. As a result, understanding the mechanisms for morphological selection of dendritic structures will be key in the development of next-generation lightweight alloys of aluminum and magnesium used in automotive and aerospace applications.

Most theoretical and experimental progress on dendritic solidification has focused on understanding the growth rate and curvature selection of 4-fold or 6-fold dendritic branches grown in isolation. The theory of microscopic solvability showed that the operating state of dendrites is established due to a singular perturbation in the surface tension anisotropy [12–16] that breaks the degeneracy established by the older Ivantsov theory [17] and allows for a unique prediction of the dendrite tip speed and radius of curvature. This theory was validated by later phase-field simulations and is consistent with some experiments [18,19]. It was the first truly self-consistent theory that elucidated the selection mechanism responsible for stabilizing dendrite branch kinetics.

Despite this progress in dendritic growth kinetics, a clear understanding of the selection principles governing the morphologies of dendritic networks or extended dendritic arrays is still lacking. Microstructures in real materials are very different from those assumed by theories of isolated dendritic growth. Most metals solidify into wide range of morphologies, including dendritic, seaweed, dense-branched, fractal-like and some that are a continuous variation between these patterns.

---

* Corresponding author.
E-mail address: amoorem@mcmaster.ca (M. Amoorezaei).

1359-6454/$36.00 © 2011 Acta Materialia Inc. Published by Elsevier Ltd. All rights reserved.
doi:10.1016/j.actamat.2011.10.006

Addressing the issue of non-equilibrium crystal morphologies found in real materials can only be achieved by understanding the fundamental mechanisms that control free-surface evolution during solidification.

This paper explores the microstructure patterns that emerge when an inherent anisotropy in a material's properties competes with process anisotropies present during solidification. This competition between anisotropies overrides the minimum stiffness criterion previously assumed to define crystal growth directions, leading to the emergence of non-dendritic patterns. Specifically, it is shown that controlling the magnitude and speed of the local thermal gradient imposed during solidification leads to a plethora of dendritic structures. Understanding such processes is key to achieving a coveted goal of materials science of custom-designing microstructure of commercial alloys.

2. Methods

2.1. Experimental procedure

As-received Mg–0.5 wt.%Al alloy was melted inside an electrical resistance furnace (LINDBERG/BLUE M) at 730 °C and poured into the cylindrical stainless steel crucible described in detail elsewhere [10]. As coolant, water (air) is splashed (blown) from below, promoting transient upward directional solidification. The crucible and surrounding insulation were designed such that in a large region at the centre of the cylindrical crucible the heat flow is unidirectional, meaning the temperature varies only in the longitudinal direction and is practically uniform in the transverse (radial) direction. The entire procedure was carried out in a protective environment of CO_2SF_6–0.5% gas. To measure the temperature at different distances from the chill wall, K-type Ni–Cr-base sheathed thermocouples were aligned at the centre of the crucible 1 mm apart from each other, starting from 1 mm above the chilling surface.

The interface velocity and temperature gradient were calculated from the time evolution of the temperature readings registered by the thermocouples. Depending on the coolant type, pressure of the cooling water, and the front position relative to the chill wall, the growth velocity range attained was 0.43–3.7 mm s^{-1} while the temperature gradient ranged from 0.6 to 4.45 K mm^{-1}.

The samples were cut in longitudinal sections, polished down to 0.05 μm and etched in a solution of 20 ml water, 20 ml acetic acid, 60 ml ethylene glycol and 1 ml HNO_3 [20] for about 5 min. The microstructure was then imaged under a light microscope.

2.2. Phase-field model

For Mg–0.5 wt.%Al we can consider the dilute limit of the phase diagram, with straight solidus and liquidus lines with a partition relation $c_s = kc_l$, where c_s (c_l) is the solute concentration at the solid (liquid) side of the interface, and k is the partition coefficient. Our two-dimensional simulations correspond to arrays of dendrites evolving on the basal plane of the hexagonal close-packed (hcp) crystal structure. Given that heat diffuses several orders of magnitude faster than impurities, latent heat is neglected and the temperature is then approximated as $T(z,t) = T_0 + G(t)(z - z_0 - \int_0^t V_p(t')dt')$, where $T(z_0,0) = T_0$ is a reference temperature, while $G(t)$ and $V_p(t)$ are the instantaneous temperature gradient and pulling speed, respectively. We model solidification under these considerations with the following sharp interface equation, where the reference concentration c_l^0 is fixed to the solute concentration at the liquid side of the planar interface c_0/k:

$$\partial_t c = D\nabla^2 c \tag{1}$$

$$c_l(1-k)v_n = -D(\partial_n c|_l - \zeta\partial_n c|_s) \tag{2}$$

$$c_l/c_l^0 = 1 - (1-k)\kappa d_0 a(\theta) - (1-k)\left(z - \int_0^t V_p(t')dt'\right)/l_T - (1-k)\beta' v_n \tag{3}$$

where $d_0 = \Gamma/\Delta T_0$ is the solutal capillary length, Γ is the Gibbs–Thomson coefficient for Al, $\Delta T_0 = |m|(1-k)c_l^0$ the freezing range, $l_T = \Delta T_0/G$ the thermal length, D the diffusivity of solute in the liquid, ζ the diffusivity of solute in the solid over that in the liquid, κ the interface curvature, and $\beta' = \beta/\Delta T_0 = 1/(\mu_k \Delta T_0)$ the kinetic coefficient. The anisotropy function $a(\theta)$ makes the interface stiffness dependent on the orientation through the anisotropy strength and misorientation angle from the crystal axis, imposing minimum stiffness at the main crystal axes directions.

The phase-field evolution equations corresponding to these sharp interface Eqs. (1)–(3), which are based on the phase-field model developed by Karma et al. [21], are given by:

$$\tau(\hat{n})\left(1 - (1-k)\frac{(z - z_{\text{int}})}{l_T}\right)\frac{\partial\phi}{\partial t} = w_0^2\vec{\nabla}\left[a(\hat{n})^2\vec{\nabla}\phi\right] + \phi - \phi^3 - \lambda(1-\phi^2)^2\left(U + \frac{z - z_{\text{int}}}{l_T}\right) \tag{4}$$

$$\left(\frac{1+k}{2} - \frac{1-k}{2}\phi\right)\frac{\partial U}{\partial t} = \vec{\nabla}\left[q(\phi)D\vec{\nabla}U - \frac{w_0}{2\sqrt{2}}(1 + (1-k)U)\hat{n}\frac{\partial\phi}{\partial t}\right] + \left(\frac{1 + (1-k)U}{2}\right)\frac{\partial\phi}{\partial t} \tag{5}$$

where

$$U = \frac{1}{1-k}\left(\frac{c/c_l^0}{(1-\phi)/2 + k(1+\phi)/2} - 1\right) \tag{6}$$

is the local supersaturation with respect to the reference point (c_l^0, T_0), $z_{\text{int}} \equiv \int_0^t V_p dt'$ is the interface position, $\tau(\hat{n}) = \tau_0 \cdot a^2(\hat{n})$ the relaxation time and $\hat{n} \equiv -\left(\vec{\nabla}\phi\right)/\left(|\vec{\nabla}\phi|\right)$ the unit vector normal to the interface. $q(\phi) = (1-\phi)/2$ is the interpolation function that governs diffusivity across the interface. The phase-field variable is set to $\phi = 1(-1)$ in the solid (liquid).

The anisotropy function $a(\hat{n}) \equiv a(\theta) = 1 + \epsilon_0 + \epsilon_6 cos[6(\theta - \theta_0)]$ is defined to represent the 6-fold crystal symmetry of the hcp structure in the basal plane, where θ is the angle between the normal to the interface and an underlying crystalline axis in the $\langle 1\,1\,\bar{2}\,0\rangle$ direction (in the basal plane) and θ_0 is the angle between the direction of heat extraction and the crystalline axis. This anisotropy function is the projection in the basal plane of the spherical harmonics representing the space group of the hcp crystal lattice: $\gamma(\theta,\phi) = \gamma_0(1 + \epsilon_{20}y_{20}(\theta,\phi) + \epsilon_{40}y_{40}(\theta,\phi) + \epsilon_{60}y_{60}(\theta,\phi) + \epsilon_{66}y_{66}(\theta,\phi) + \cdots)$ where ϵ_{20}, ϵ_{40}, ϵ_{60} and ϵ_{66} are constant coefficients weighting the contribution of each of the spherical harmonic functions:

$$\begin{aligned}
y_{20}(\theta,\phi) &= \sqrt{5/16\pi}[3cos^2(\theta) - 1] \\
y_{40}(\theta,\phi) &= 3/(16\sqrt{\pi})[35cos^4(\theta) - 30cos^2(\theta) + 3] \\
y_{60}(\theta,\phi) &= \sqrt{13}/(32\sqrt{\pi})\big[231cos^6(\theta) - 315cos^4(\theta) \\
&\quad + 105cos^2(\theta) - 5\big] \\
y_{66}(\theta,\phi) &= \sqrt{6006/64\sqrt{\pi}}\big[sin^6(\theta)cos(\phi)\big] \qquad (7)
\end{aligned}$$

while θ and ϕ are the inclination (or elevation) and azimuth spherical coordinate angles, respectively. The 2-D surface energy anisotropy function projected in the basal plane is obtained by substituting $\theta = \frac{\pi}{2}$, $\epsilon_{20} = -0.026$ and $\epsilon_{66} = 0.003$ [22]. The contributions of ϵ_{40} and ϵ_{60} can be neglected [22]. We then obtain $\gamma(\phi) = 1.008 + 0.002\cos(6\phi)$. The stiffness anisotropy function $a(\phi)$ is therefore taken as:

$$\begin{aligned}
&a(\phi) = \left(\gamma(\phi) + \frac{\partial^2\gamma(\phi)}{\partial\phi^2}\right)/\gamma_0 = 1 + \epsilon_0 - \epsilon_6\cos(6\phi); \\
&\epsilon_0 = 0.008,\ \epsilon_6 = 0.07 \qquad (8)
\end{aligned}$$

Our model also includes thermal noise to promote side-branching, but for brevity the corresponding terms and explanation of their origin are absent in the model presented in this section. Details on the inclusion of thermal noise in the model can be found in Ref. [10].

The material parameters employed in this work are presented in Table 1. The misorientation angle between the thermal gradient direction and crystalline axis was set at $\theta_0 = \pi/6$, the maximum misorientation for hexagonal dendrites growing on the basal plane in the $(\langle 1\,1\,\bar{2}\,0\rangle)$ direction. The phase-field equations were simulated utilizing the adaptive mesh refinement (AMR) scheme developed by Provatas et al. [23–25].

Table 1
Material parameters defining the MgAl system. m is the liquidus slope, c_0 the alloy composition, k the partition coefficient, D the diffusivity of solute in the liquid, ζ the diffusivity of solute in the solid over that in the liquid, Γ the Gibbs–Thomson coefficient, ϵ_0 the constant in the projected 2-D anisotropy function and ϵ_6 the anisotropy strength.

$\lvert m\rvert$ (K wt.%$^{-1}$)	c_0 (wt.%)	k	D (μm^2 s^{-1})	ζ	Γ (K μm)	ϵ_0	ϵ_6
5.5	0.5	0.4	1800	10^{-4}	0.62	0.008	0.07

3. Morphological transitions

Previous experimental and numerical investigations of non-axially growing dendrites in cubic materials, where the imposed thermal gradient was misaligned with respect to the main axes of the crystalline structure, offer insight into the effect that competing preferred growth directions have on the orientation that dendrites eventually select [26–32]. There is evidence of the primary dendrite arm/cellular spacing being affected by the relative direction of the imposed thermal gradient and preferred crystalline orientation, even for the same growth velocity, temperature gradient strength and composition [26–28,31]. There is also evidence that the distribution of interdendritic phases could be greatly influenced by the misorientation angle as the secondary arms start to overtake the primary ones [26].

Molecular dynamics simulations conducted by Sun et al. [22] reveal that magnesium is weakly anisotropic and therefore the dendrites tend to alter their orientation if heat extraction through a sample is imposed in a direction that differs from that of one of the main crystal axes. This makes magnesium alloys an ideal system to explore the morphologies arising from these competing growth directions. Sun et al. [22] also show that for magnesium-base alloys dendrites grow preferentially in the $\langle 1\,1\,\bar{2}\,0\rangle$ direction on the basal plane.

Dendritic morphologies in Mg–Al alloys obtained through extensive phase-field simulations are organized via the morphology diagram shown in Fig. 1. Several regimes can be identified in the figure. The transitions between these regimes are gradual, and hence no sharp limit can be defined between them. Nevertheless, in order to guide our discussion we have included empirically determined dashed lines separating the main regimes of observed morphologies. At velocities just above the planar-cellular instability (Mullins–Sekerka) [33], cells grow in the direction of the thermal gradient. As the growth speed increases towards the cell-to-dendrite transition, cells begin to deviate towards the preferred crystallographic direction until the primary stalks grow along a main crystalline axis, in agreement with the findings of Trivedi et al. [27]. At velocities below the vertical dashed line, the growth orientation is more sensitive to the strength of the thermal gradient. In the dendritic region, lower temperature gradients favour growth along the direction of the main crystalline axes, whereas higher thermal gradient strengths above the horizontal dashed line favour a seaweed microstructure where dendrites tips continuously split and change orientation, consistent with previous experiments [34] and the simulations [35]. Note that at pulling speeds lower than the vertical dashed line, the thermal gradient required to favour seaweed structures increases with pulling speed, making the horizontal dashed line curved. The dotted line represents the cell-to-dendrite transition velocity wherein $l_D = kl_T$ [36].

At higher growth speeds the morphology becomes less sensitive to the thermal gradient and the resulting

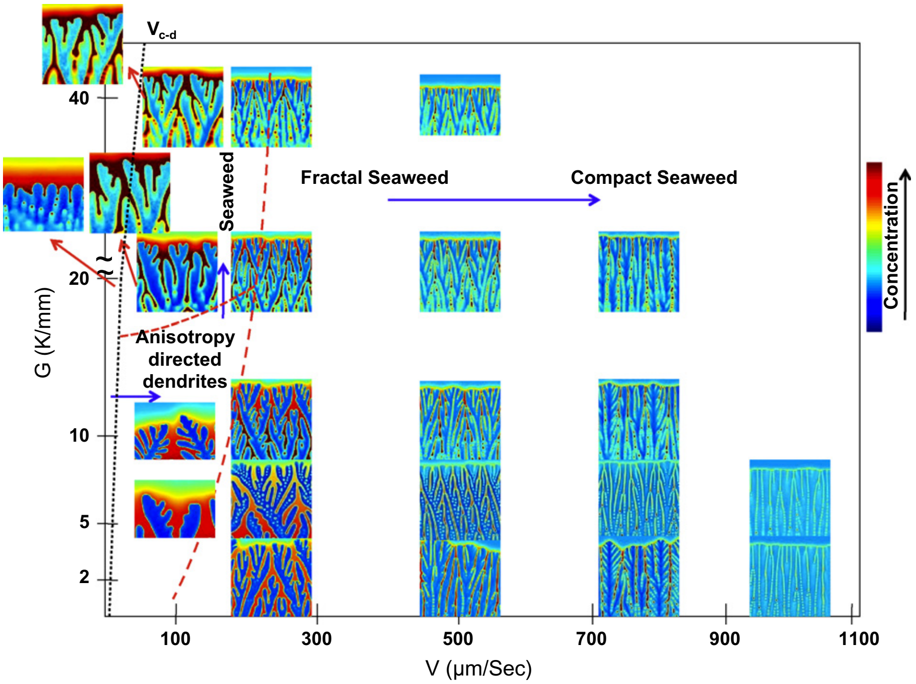

Fig. 1. Phase diagram of simulated crystal morphologies in directional solidification of Mg–0.5 wt.%Al alloy. The colour bar represents the solute concentration and the dashed lines estimate the boundary between the different regimes. The dotted line represents the cell-to-dendrite transition velocity. Note the change in scale in the temperature gradient axis (*Y*-axis) at $G = 20\ \mathrm{K\ mm^{-1}}$. The width of each subsection corresponds to 250 μm.

morphology, termed “seaweed”, shows comparable influences from the competition of the heat extraction direction and the preferred crystalline axes. To date, it has not been shown that a directionally solidified tilted dendrite in an alloy system growing on one of the crystallographic axes can transition to a seaweed as the pulling speed is increased, rather than remaining stable until the absolute stability limit. Evidence of the transition from dendrite to seaweed has been reported when the thermal gradient or the tilt angle is sufficiently increased [28–30,32,34,35]. Only dendrite-to-dendrite transitions from one to the other available dendrite state, and the formation of doublon dendrites, has been previously observed as the front speed is increased from the initial dendritic region [37,38]. The dendrite-to-seaweed transition occurs as the curvature contribution of the tip undercooling, which increases with velocity, becomes comparable to the solutal undercooling, leading to the alternating tip splitting and change of the tip growth direction, a characteristic inherent in degenerate or fractal seaweeds [37,39]. The transition from dendrite to seaweed is highly dependent on the anisotropy strength and material parameters, and shifts to much higher speeds for largely anisotropic systems. For example, as shown in Fig. 2, for a hexagonal system with the same parameters except $\epsilon = 35\epsilon_6$ and $\Gamma = 0.14\ \mathrm{K\ \mu m}$, we find the dendrite-to-seaweed transition at $V = 3000\ \mathrm{\mu m\ s^{-1}}$, almost 15 times higher than that for the system studied herein. Note that the thermal gradient induced transition (the equivalent of horizontal dashed line in Fig. 1) also shifts to much higher temperature gradients, implying the strong dependence of the transition on the anisotropy strength.

At the highest growth velocities probed, the direction of the temperature gradient dominates and columnar (forward-directed) seaweeds form independently of the strength of the temperature gradient. Beyond the limit of degenerate seaweeds, the spacing between the two advancing seaweed tips is a decreasing function of velocity as depicted in Fig. 3. The maximum distance between the tips before either undergoes an instability, λ_t (see Fig. 3), follows a power-law relationship with respect to the pulling speed with the slope of the line in logarithmic scale

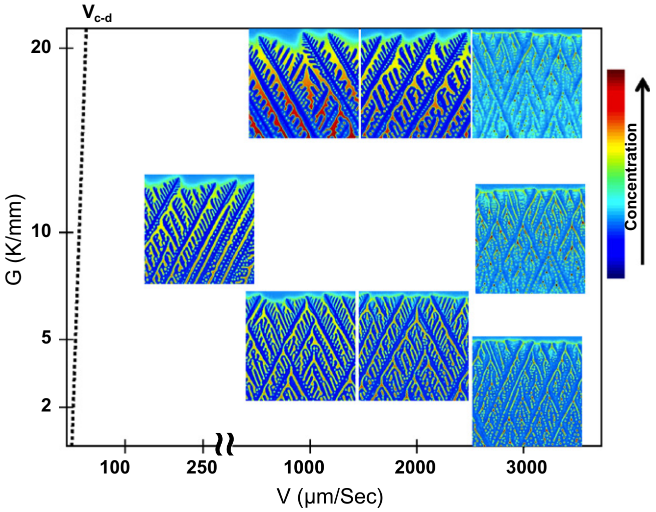

Fig. 2. Phase-field-generated phase diagram of morphological transition at a range of growth conditions in directional solidification of a strongly anisotropic hexagonal system.

corresponding to −0.46. This value is in conformity with the measured instability wavelength of a single seaweed tip by Utter et al. [34] and also with the instability wavelength of a flat interface [33], $\lambda \alpha V^{-0.5}$. The two advancing seaweed tips reduce the spacing between them as the pulling velocity is increased until the wavelength becomes comparable to the width of the stem. This gives rise to the formation of a "compact seaweed" microstructure, where the tips have less curvature and branching is less frequent. An example of such structure can be found at the rightmost part of Fig. 1. The transition from fractal to compact structure has been previously reported by Brener et al. [40] for pure materials. It is noteworthy that at $V = 750\ \mu\text{m s}^{-1}$ and $G = 2\ \text{K mm}^{-1}$ a combination of doublon dendrites with developed sidebranches and seaweed structures (dendritic-like structure with unstable tips) can be observed. The formation of sidebranches is attributed to the larger spacing available between the dendrites due to the lower operating temperature gradient.

We assume that the surface energy anisotropy is the only factor that interplays with the heat flow direction to establish the growth orientation of the stalks. This is in contrast with the linear stability analysis provided by Sekerka [41] and the weakly nonlinear stability analysis of Young [42], which imply that the interface attachment kinetics governs the growth orientation selection in the vicinity of the cellular threshold limit. However, the effect of surface tension anisotropy is largely underestimated in these theories due to the linear nature of their analyses. In the fully nonlinear regime, the surface energy anisotropy becomes more important and needs to be considered. More importantly, in metallic systems the kinetic coefficient is three orders of magnitude smaller than in organic, analogous to metals, e.g. SCN and pivalic acid alloys [19,30,43], which are commonly exploited in dendritic growth experiments. Interface kinetics are thus not very relevant for such transition in metal alloys. Even for the highest growth velocity studied herein, the curvature contribution to the undercooling is almost two orders of magnitude larger than that of kinetic attachments. Moreover, Okada et al. [29] reported observing stem rotation towards the crystalline axis as the velocity is increased in steel containing Ni and Cr impurities, while neglecting kinetic effects.

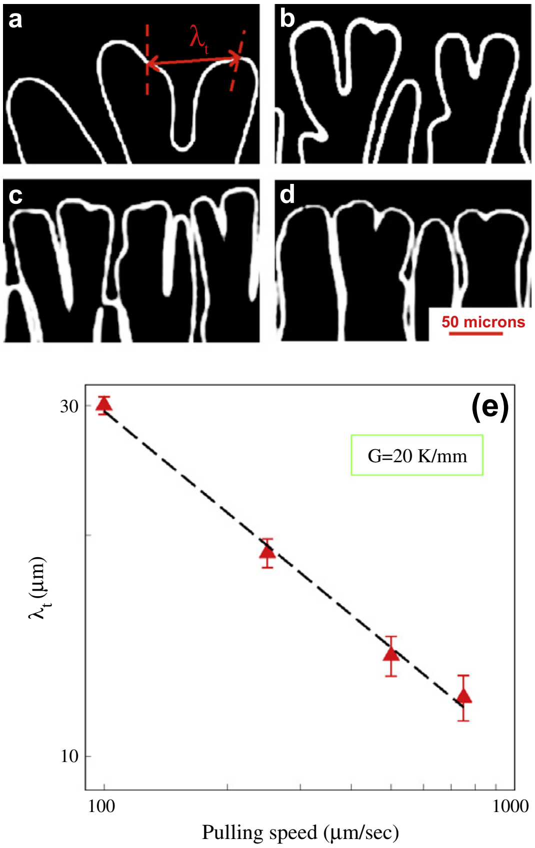

Fig. 3. Different seaweed morphologies at $G = 20\ \text{K mm}^{-1}$ and pulling speeds of (a) 100, (b) 250, (c) 500 and (d) 750 $\mu\text{m s}^{-1}$. The white line represents the interface between phases. The graph plots the tip spacing against the pulling speed and follows a power-law relationship with an exponent of −0.46.

A criterion for a quantitative determination of the velocity and thermal gradient dependent dendrite-to-seaweed transitions will be sought in an forthcoming publication. This work is based on the tip undercooling variation for different growth directions. Based on our results and considering the dissimilarity of microstructures of thermal gradient-driven seaweeds and velocity-driven seaweeds, it is not clear if a unified criterion to self-consistently characterize the velocity-induced and gradient-induced regimes exists.

Remarkably, the morphologies shown in Fig. 1 can be obtained in the same crystal if different sections of the materials have locally different thermal conditions—a situation that is quite common in experiments. This will lead to each of these sections having a different growth speed and thermal gradient. Based on our findings, this will result in different sections of the material solidifying into different morphologies as depicted in Fig. 1. To demonstrate how to achieve a spectrum of the morphologies as shown in Fig. 1 in a single-crystal material, we simulated a tilted dendrite at the right corner of a channel as shown in Fig. 4. As the tip moves up, a secondary arm grows freely towards the left boundary of the channel, perpendicularly to the direction of the thermal gradient. The tertiary arms emerging from it grow in the same direction as the initially dendrite branch (upward), but at a higher undercooling (than the parent stalk) as they are retarded since they emerge from the secondary branch. In order to catch up and reach the steady-state tip undercooling, these tertiaries grow at a very rapid rate. The resulting morphology shown in Fig. 4 exhibits spatial transitions from dendrite to seaweed, and to partially columnar going from right to left in the figure, which corresponds to increasing front speed.

The interplay of different sources of anisotropies and their influence on the microstructure that emerges has been investigated in the work by Haxhimali et al. [9], where they varied the strength of two composition-dependent anisotropy parameters and showed that the orientation of

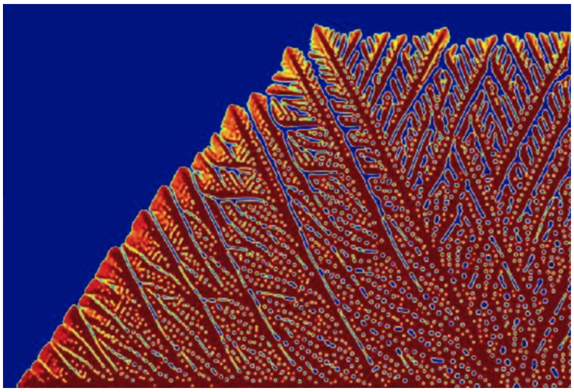

Fig. 4. Phase-field simulation of a single crystal with branches growing at different velocities, promoting a spectrum of morphologies. The growth velocity increases towards the left, leading to the formation of seaweed and columnar structures. The image is a subsection of the entire domain. The width corresponds to 300 μm and the temperature gradient is $G = 10\ \mathrm{K\ mm^{-1}}$. The colours represent solid (red) and liquid (blue) phases. (For interpretation of the references to colour in this figure legend, the reader is referred to the web version of this article.)

equiaxed dendrites varies continuously. Their results, however, do not provide the ability to control the emerging microstructure for a given alloy composition, since the anisotropy parameters are implicitly controlled by concentration. Our results are similar to Haxhimali et al.'s in that the interplay of two sources of anisotropies is shown to lead to a continuous orientation variation. However, since the cooling rate and direction in our directional solidification experiments and simulations are adjustable control parameters, the emerging microstructure can be controlled for a given alloy composition, as needed.

Our results on orientation selection are supported by our directional solidification experiments in magnesium-base systems. Fig. 5 shows a typical dendritic microstructure of a directionally solidified Mg–0.5 wt.%Al alloy. The initial morphology encompasses two different grains, highlighted in the figure. The right grain starts misoriented with respect to the thermal gradient but after a short transient undergoes a transition towards the direction of the thermal gradient. The transient in the left grain is not as clear, but it also ends up orienting with the thermal gradient after a short transient of similar duration. In terms of the phase diagram in Fig. 1, the temperature gradient strength of this experiment falls in the lower range of values. The velocity of the experimental front, however, is beyond the highest value shown in the phase diagram, which leads to a columnar-type growth in the upward (gradient) direction. In casting situations, as in our experiments, the interface velocity at the chill surface is significantly higher than the values probed in our simulations. In this regime, we also expect kinetic effects to become important.

Our 2-D simulations predict the same qualitative morphological orientation variations with growth speed as our 3-D experiments, the quantitative difference being due to the discrepancy in dimensionality. This is analogous to recent results of Gurevich et al. [44], where primary spacing results do not change qualitatively between 2-D and 3-D directional solidification simulations and experiments. We are thus confident that 3-D morphological structures will present qualitatively the same transitions as predicted by our 2-D simulated morphologies, with the critical transition values appropriately shifted. Specifically, given that the tip undercooling for a 3-D steady-state cell falls below that of the equivalent 2-D shape [44], we expect the transition velocity and the transition temperature gradient to shift to lower values for a 3-D shape.

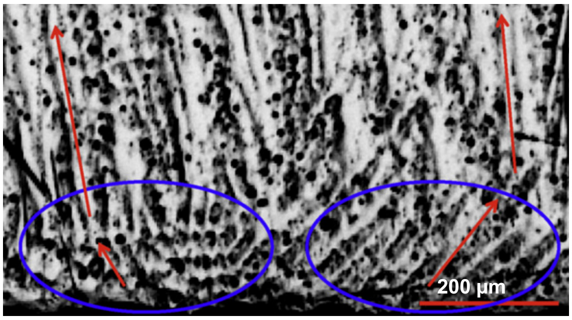

Fig. 5. Dendritic microstructure of a directional solidification of Mg–0.5 wt.%Al alloy. Two initial grains misoriented with respect to the upward thermal gradient are shown. The initially misoriented dendrites tilt towards the heat flow direction after a short transient time.

In summary, we have presented new results from simulations and experiments that demonstrate the emergence of a spectrum of dendritic and fractal-like solidification patterns in alloys when anisotropies in the processing environment compete with the inherently anisotropic properties of the material. It is noted that we expect our results to hold in three dimensions. Our work suggests that the morphologies arising from varying the solidification rate are much more complex than previously thought. Controlling the patterns that form in microstructures by altering processing conditions provides new opportunities to control the final morphology, spacing and distribution of secondary phases in materials, which is crucial for optimizing the mechanical properties of alloys for a range of applications, a topic crucial to the development of next-generation lightweight alloys for automotive and aerospace industries.

Acknowledgements

The authors thank the Natural Science and Engineering Research Council of Canada and Novelis Global Technology Centre for financial support of this project. We also thank Nana Ofori-Opoku, Micheal Greenwood and Jeff Hoyt for useful discussions.

References

[1] Langer JS. Rev Mod Phys 1980;52:1–28.

[2] Burden MH, Hunt JD. J Cryst Growth 1974;22:109–16.

[3] Hunt JD. Cellular and primary dendrite spacings. In: Solidification and casting of metals. London: The Metals Society; 1979. p. 3–9.

[4] Ben-Jacob E, Garik P. Nature 1990;343:523–30.

[5] Losert W, Shi BQ, Cummins HZ, Warren JA. Phys Rev Lett 1996;77:889–91.
[6] Trivedi R, Liu S, Williams S. Nat Mater 2002;1:157–9.
[7] Granasy L et al. Nat Mater 2003;2:92–6.
[8] Granasy L, Pusztai T, Borzsonyi T, Warren JA, Douglas JF. Nat Mater 2004;3:645650.
[9] Haxhimali T, Karma A, Gonzales F, Rappaz M. Nat Mater 2006;5:660–4.
[10] Amoorezaei M, Gurevich S, Provatas N. Acta Mater 2010;58:6115–24.
[11] Gurevich S, Amoorezaei M, Provatas N. Phys Rev E 2010;82:051606.
[12] Ben-Jacob E, Goldenfeld N, Kotliar BG, Langer JS. Phys Rev Lett 1984;53:2110–3.
[13] Kessler DA, Koplic J, Levine H. Phys Rev A 1985;31:1712–7.
[14] Kessler D, Koplik J, Levine H. Adv Phys 1988;37:255–339.
[15] Barbieri A, Langer JS. Phys Rev A 1989;39:5314–25.
[16] Ben Amar M, Brener E. Phys Rev Lett 1993;71:589–92.
[17] Ivantsov GP. Dokl Akad Nauk SSSR 1947;58:567–9.
[18] Karma A, Rappel WJ. Phys Rev E 1996;53:3017–20.
[19] Bragard J, Karma A, Lee YH, Plapp M. Interface Sci 2002;10:121–36.
[20] Pettersen K, Lohne O, Ryum N. Metall Trans A 1990;21A:221–30.
[21] Echebarria B, Folch R, Karma A, Plapp M. Phys Rev E 2004;70:061604.
[22] Sun DY et al. Phys Rev B 2006;73:024116.
[23] Provatas N, Goldenfeld N, Dantzig J. Phys Rev Lett 1998;80:3308–11.
[24] Athreya BP, Goldenfeld N, Dantzig JA, Greenwood M, Provatas N. Phys Rev E 2007;76:056706.
[25] Ofori-Opoku N, Provatas N. Acta Mater 2010;58:2155–64.
[26] Grugel RN, Zhou Y. Metall Trans A 1989;20A:969–73.
[27] Trivedi R, Seetharaman V, Eshelman MA. Metall Trans A 1991;22A:585–93.
[28] Borisov AG, Fedorov OP, Maslov VV. J Cryst Growth 1991;112:463–6.
[29] Okada T, Saito Y. Phys Rev E 1996;54:650–5.
[30] Akamatsu S, Ihle T. Phys Rev E 1997;56:4479–85.
[31] He G, Li J, Mao X, Fu H. J Mater Sci Technol 1998;14:200–4.
[32] Deschamps J, Georgelin M, Pocheau A. Phys Rev E 2008;78:011605.
[33] Mullins WW, Sekerka RF. J Appl Phys 1964;35:444–51.
[34] Utter B, Ragnarsson R, Bodenschatz E. Phys Rev Lett 2001;86:4604–7.
[35] Provatas N, Wang Q, Haataja M, Grant M. Phys Rev Lett 2003;91:155502.
[36] Trivedi R, Kurz W. Int Mater Rev 1994;39:49–74.
[37] Akamatsu S, Faivre G, Ihle T. Phys Rev E 1995;51:4751–73.
[38] Utter B, Bodenschatz E. Phys Rev E 2005;72:011601.
[39] Utter B, Bodenschatz E. Phys Rev E 2002;66:051604.
[40] Brener E, Muller-Krumbhaar H, Temkin D, Abel T. Solid State Ionics 2000;131:23–33.
[41] Coriell SR, Sekerka RF. J Cryst Growth 1976;34:157–63.
[42] Young GW, Davis SH, Brattkus K. J Cryst Growth 1987;83:560–71.
[43] Xia ZG, Sun DY, Asta M, Hoyt JJ. Phys Rev B 2007;75:012103.
[44] Gurevich S, Karma A, Plapp M, Trivedi R. Phys Rev E 2010;81:011603.